

GEDDnet: A Network for Gaze Estimation with Dilation and Decomposition

Zhaokang Chen and Bertram E. Shi, *Fellow, IEEE*

Abstract—Appearance-based gaze estimation from RGB images provides relatively unconstrained gaze tracking from commonly available hardware. The accuracy of subject-independent models is limited partly by small intra-subject and large inter-subject variations in appearance, and partly by a latent subject-dependent bias. To improve estimation accuracy, we propose to use dilated-convolutions in a deep convolutional neural network to capture subtle changes in the eye images, and a novel gaze decomposition method that decomposes the gaze angle into the sum of a subject-independent gaze estimate from the image and a subject-dependent bias. To further reduce estimation error, we propose a calibration method that estimates the bias from a few images taken as the subject gazes at only a few or even just a single gaze target. This significantly reduces calibration time and complexity. Experiments on four datasets, including a new dataset we collected containing large variations in head pose and face location, indicate that even without calibration the estimator already outperforms state-of-the-art methods by more than 6.3%. The proposed calibration method is robust to the location of calibration target and reduces estimation error significantly (up to 35.6%), achieving state-of-the-art performance with much less calibration data than required by previously proposed methods. The dataset is available at <http://nisl gaze.ust.hk> and the source code is available at <https://github.com/czk32611/GEDDnet>.

Index Terms—Appearance-based gaze estimation, Eye tracking, Calibration, Dataset, Deep neural network.

1 INTRODUCTION

EYE gaze has been used successfully in many promising applications, such as human-computer interfaces [1], [2], human-robot interaction [3], health care [4], virtual reality [5], [6] and social behavioral analysis [7], [8]. These successful applications have attracted more and more attention to eye tracking.

To date, most commercial eye trackers have relied upon active illumination, e.g. pupil center corneal reflections (PCCR) based eye tracker used infrared illumination. While these eye trackers provide high accuracy, they are costly, commonly used in indoor laboratory settings, and place strong constraints on users' head movements. To alleviate the constraints on head movement, researchers have proposed many novel methods [9], [10], [11], [12], [13]. Unfortunately, these eye trackers typically fail outdoors due to strong interference from the sun's infrared radiation.

Appearance-based gaze estimation estimates gaze direction from RGB images, providing relatively unconstrained eye tracking and can be used both indoors and outdoors. It requires only commonly available off-the-shelf cameras. However, obtaining high accuracy is challenging due to the variability caused by factors such as changes in appearance, illumination and head pose [14]. The application of deep convolutional neural networks (CNNs) has reduced estimation error significantly [15]. Trained using a large number of high quality real and synthetic datasets covering a wide range of these variations [15], [16], [17], [18], [19], [20], [21], [22], [23], [24], deep CNNs can learn to compensate for much

of the variability [19], [25], [26], [27], [28], [29], [30], [31], [32], [33].

Despite these improvements, the estimation error of subject-independent appearance-based approaches is still not as low as that achieved by using active illumination, e.g. $\sim 5^\circ$ vs $\sim 1^\circ$. Further work must be done to reduce this error.

This paper proposes two techniques to improve accuracy. First, we propose to use dilated-convolutions, rather than max-pooling in the deep CNNs. While dilated-convolutions have been widely used for pixel-wise tasks, such as segmentation [34], [35], they have rarely been used for more global tasks, like regression or classification. We show that by learning high-level features at high resolution, dilated-convolutions better capture the subtle changes in eye appearance as gaze changes.

Second, we decompose gaze estimates into the sum of a gaze estimate that is estimated by a subject-independent deep dilated CNN and a subject-dependent bias. During training, we learn both the subject-independent gaze estimator and the subject-dependent bias. During testing, we can either set the bias term to zero if no calibration data are available, or estimate the bias from calibration images. The gaze decomposition is similar in spirit to the person-dependent latent parameters proposed by Lindén et al. [36], but there are several important differences. First, we use much fewer parameters (two v.s. six). Second, the parameters are introduced in the output layer, rather than fed to the last fully-connected layers. This results in far superior performance when only few calibration images are available. Reducing the size and complexity of the calibration set makes calibration easier and less time-consuming.

With calibration, there is a trade-off between the complexity of the calibration set and accuracy. Simpler cali-

• Z. Chen and B.E. Shi are with the Department of Electronic and Computer Engineering, the Hong Kong University of Science and Technology, Hong Kong SAR.
E-mail: zchenbc@connect.ust.hk, eebert@ust.hk

bration sets are desirable, as they are easier to collect, but result in lower accuracy. The challenge we address is to achieve the best accuracy with the lowest complexity. We consider two measures of calibration set complexity: the number of different gaze targets and the number of images per target. The larger the values, the more complex the calibration set. We focus on simple calibration set as it is more convenient for the user and is more widely applicable. For best performance, the multiple images for each gaze target should contain variation in head pose.

This paper has four main contributions. First, we propose an approach that outperforms the state-of-the-art by more than 6.3% on the MPIIGaze and the EYEDIAP datasets. Second, our network outperforms the state-of-the-art calibration algorithms for low complexity calibration sets. Third, we provide an analysis explaining why the gaze decomposition method results in better performance. Fourth, we describe a new large-scale eye tracking dataset, **NISLGaze**, which includes larger variability in head pose and location than other datasets. Our method outperforms the state-of-the-art in this more complex and realistic setting.

2 RELATED WORK

2.1 Appearance-Based Gaze Estimation

Past approaches to appearance-based gaze estimation have included Random Forests [22], k-Nearest Neighbors [22], [37], and Support Vector Regression [37]. More recently, the use of deep CNNs to appearance-based gaze estimation has received increasing attention. Zhang *et al.* proposed the first deep CNN for gaze estimation in the wild [14], [15], which gave a significant improvement in accuracy.

Considering regions of the face outside the eyes has further improved accuracy. For example, Krafka *et al.* proposed a CNN with multi-region input, including an image of the face, images of both eyes and a face grid [19]. Parekh *et al.* proposed a similar multi-region network for eye contact detection [30]. Zhang *et al.* proposed a network that takes the full face image as input and adopts a spatial weighting method to emphasize features from particular regions of the face [33].

Other work has focused on how to extract better information from eye images. Cheng *et al.* developed a multi-stream network to address the asymmetry in gaze estimation between left and right eyes [26]. Yu *et al.* proposed to estimate the locations of eye landmark and gaze directions jointly [38]. Park *et al.* proposed to learn an intermediate pictorial representation of the eyes [39]. Lian *et al.* proposed to use using images from multiple cameras [28]. Xiong *et al.* proposed mixed effects neural networks to tackle the problem caused by the non *i.i.d.* natural of eye tracking datasets [32].

Still others have sought to improve robustness to the change in head pose. Deng and Zhu estimated the head pose in camera-centric coordinates and the gaze directions in head-centric coordinates, and then combined them geometrically [27]. Ranjan *et al.* applied a branching architecture, whose parameters were switched according to a clustering of head pose angles [31]. Palmero *et al.* proposed to used 3D shape cue of the face [29].

2.2 Calibration

PCCR-based eye trackers typically require an initial calibration before they are used. The user gazes sequentially at multiple gaze targets (typically nine targets on a 3×3 grid) [40]. This enables the subject-specific parameters of a geometric 3D eye model to be estimated.

Calibration for appearance-based methods has received relatively little attention to date. To the best of our knowledge, the first implementation of personal calibration was in iTracker [19]. After training a subject-independent network, this system was calibrated by training a subject-dependent Support Vector Regressor on the features extracted from the last fully-connected layer of the subject-independent network. It used images collected as the subject gazed at 13 different locations as the calibration set. Error was reduced by about 20% when calibrated on the full set, but increased when only calibrated on a subset of 4 locations, most likely due to overfitting. Lindén *et al.* proposed a network that had some subject-dependent latent parameters [36]. During training, these parameters were learned from the training data. During testing, these parameters were re-estimated by minimizing the estimation error over a calibration set. The calibration set required 45 to 100 images collected as the subject gazed at multiple points. Liu *et al.* learned a homogeneous linear transformation matrix to warp the estimates from a subject-independent estimator [41]. Zhang *et al.* learned a third-order polynomial function to warp the estimates [42].

The past work described above assumed high complexity calibration sets. Only recently has attention been paid to reducing the complexity of the calibration set. Liu *et al.* proposed a differential approach for calibration, where they trained a subject-independent Siamese network to estimate the difference between the gaze angles of two images of the same subject [41], [43]. Yu *et al.* proposed gaze redirection synthesis, which augment the calibration samples using a generative adversarial network (GAN) to fine-tune a subject-independent estimator [44]. Park *et al.* proposed FAZE, which trained the last multi-layer perceptron using meta-learning to learn good initial weights that can adapt to a few samples [45]. These works only require a few calibration samples gazing at different gaze targets.

In comparison to the work described in the previous two paragraphs, we only adapt the subject-specific bias during calibration. Our experimental results indicate that this is the dominant factor that degrades the accuracy. Our proposed method achieves better accuracy with low complexity calibration sets. Other more complex algorithms eventually outperform ours, but only for very large calibration datasets where subjects are required to gaze at a prohibitively large number of targets.

2.3 Eye Tracking Datasets

Available datasets for training appearance-based gaze estimators can be categorized as either real-world or synthetic based on the image generation process, and as either eye-only or full-face based on image content.

Real-world datasets contain images of real people taken as they gaze at different points in the environment. ColumbiaGaze contains images of 56 subjects with a discrete

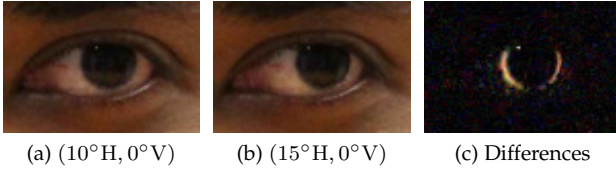


Fig. 1. Images of two left eyes and their difference from the Columbia Gaze dataset [21]. (a) Image with 10° horizontal and 0° vertical gaze angle. (b) Image with 15° horizontal and 0° vertical gaze angle. (c) The absolute difference between (a) and (b) (the value is scaled for better illustration).

set of head poses and gaze targets [21]. EYEDIAP contains videos of 16 subjects gazing at targets on a screen or floating in 3D [17]. MPIIGaze contains images of 15 subjects when using their laptops [15]. GazeCapture contains images of 1,474 subjects taken while they were using tablets [19]. RT-GENE contains images of 15 subjects behaving naturally [16]. Commercial eye tracking glasses were used to provide ground truth gaze direction, and a GAN was used to remove the eye tracking glasses from the images.

To provide samples with larger variations in head pose and appearance, some researchers have generated datasets of synthetic images. The UT-multiview [22] and UnityEyes [24] datasets used real-world images and 3D eye region models to render eye-only images at arbitrary head poses and gaze directions. Recently, GANs have been used to generate photorealistic samples [18], [20], [23].

We describe here a new dataset, NISLGaze, which contains full-face images of 21 subjects. NISLGaze contains larger variability in face locations and head poses than existing datasets. This variability makes it useful for estimating the performance of appearance-based gaze estimators in relatively unconstrained real-world settings.

3 METHODOLOGY

3.1 Spatial Resolution

Image differences due to gaze shifts can be subtle, especially if the head remains fixed. As shown in Fig. 1, eye images with gaze angles differing by 5° horizontally differ at only a few pixels. Intuitively, extracting high-level features at high resolution can better capture these subtle differences. However, most current CNN architectures use multiple downsampling layers, e.g. convolutional layers with large strides and max-pooling layers, which reduce spatial resolution. This is useful for classification, as the network tolerates small variations in position. However, for gaze estimation, valuable information is lost.

To address this problem, we propose to replace convolutional/downsampling layers by dilated-convolutional layers. Dilated-convolutions increase receptive field (RF) size while keeping the number of parameters manageable by inserting spaces (zeros) between weights. Let (x, y) and (n, m) represent spatial position, and k indicate the feature map. Given an input feature map $u(x, y, k)$, a weight kernel w_{nmk} of size $N \times M \times K$, a bias term b , and dilation

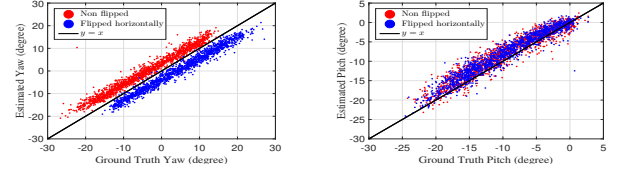


Fig. 2. Scatter plots of the estimated gaze angles versus the ground truth of subject p06 from MPIIGaze.

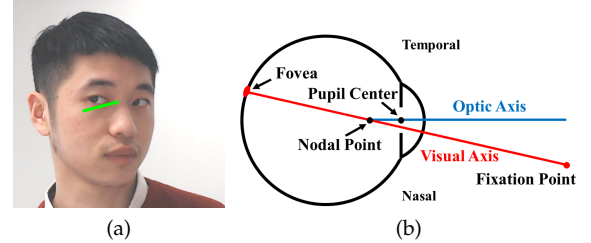


Fig. 3. Overview. (a) Appearance-based gaze estimation estimates the gaze angles (pitch and yaw) from RGB images. However, there are some factors not observable from the images, such as (b) the subject-dependent offset between the optic axis and visual axis.

rates (r_1, r_2) , the output feature map $z(x, y)$ of a dilated-convolutional operation can be calculated by

$$z(x, y) = \sum_{k=1}^K \sum_{m=0}^{M-1} \sum_{n=0}^{N-1} u(x + nr_1, y + mr_2, k) w_{nmk} + b. \quad (1)$$

The dilation rates (r_1, r_2) determine the amount by which the size of RF increases.

3.2 Subject-Dependent Bias

Fig. 2 compares the gaze angles estimated by a subject-independent estimator [25] and the ground truth for one subject (p06) from MPIIGaze [15]. The scatter plots indicate that there is a bias between the estimates and ground truth angles, which is quite constant across gaze angles. When the image are flipped horizontally, the yaw bias changes sign, but the pitch bias stays similar.

The bias has two sources: first, there are components of gaze that vary from subject to subject that cannot be estimated from appearance. For example, as shown in Fig. 3(b), there is a deviation between the visual axis (the line connecting the nodal point with the fovea) and the optic axis (the line connecting the nodal point with the pupil center) of an eye, which varies from person to person [40], [46]. Second, there may be changes in appearance between subjects that are also correlated with gaze shift.

Fig. 4 analyzes the error of the subject-independent estimator [25] across subjects on MPIIGaze in leave-one-subject-out cross-validation. Fig. 4 show the means and standard deviations (SDs) of the yaw and pitch error, for different subjects and for both the original and horizontally flipped images. These results show that in both yaw and pitch angles, the errors are generally biased. The bias varies widely across subjects. When a image is horizontally flipped, the yaw bias typically has similar magnitude but a different sign, while the pitch bias remains similar. The mean squared bias across subjects (16.2 deg^2) exceeds the

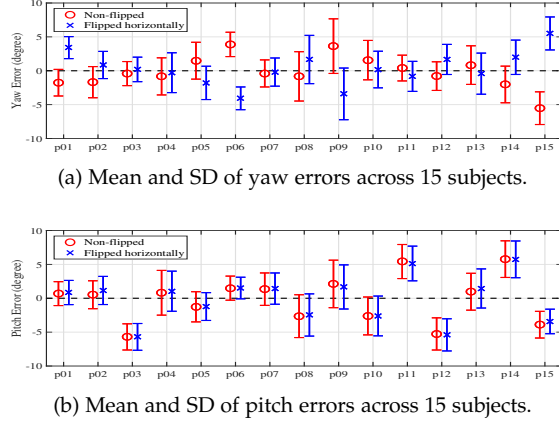


Fig. 4. Error analysis of our subject-independent estimator [25] on the MPIIGaze dataset [15] for (a) yaw and (b) pitch. Circles and crosses indicate the means. Error bars indicate standard deviations.

mean intra-subject variance (12.9 deg^2), indicating that the bias is a significant contributor to the error.

Motivated by these findings, for the j^{th} image of the i^{th} subject in a dataset, $X_{i,j}$, we decompose our gaze estimate $\hat{g}(X_{i,j}) \in \mathbb{R}^2$ (yaw, pitch) into the sum of a subject-independent estimate $\hat{t}(X_{i,j}; \Phi) \in \mathbb{R}^2$ and a subject-dependent bias $\hat{b}_i \in \mathbb{R}^2$:

$$\hat{g}(X_{i,j}) = \hat{t}(X_{i,j}; \Phi) + \hat{b}_i, \quad (2)$$

where Φ denotes the parameters of a dilated CNN for estimating \hat{t} , as described below.

3.3 Preprocessing

We adopt the data normalization method in [47]. This method rotates and translates a virtual camera so that it faces a reference point on the face from a fixed distance and cancels out the roll angle of the head. The images are normalized by perspective warping, converted to gray scale and histogram-equalized. The ground truth gaze angles are also normalized correspondingly. We use dlib [48] and OpenFace [49] to detect the facial landmarks.

We align the images based on detected landmarks. The face images are aligned so that the center of each eye is at a fixed location in the resulting images. The eye images are aligned so that the eye corners are at fixed locations.

3.4 Architecture

The architecture of our proposed network implementing $\hat{t}(X_{i,j}; \Phi)$ is presented in Fig. 5. The general architecture is inspired by iTracker [19], but differs in that we do not use the face grid as input, and in that we replace some convolutional and max-pooling layers with dilated-convolutional layers.

Our network takes images of the face and of both eyes as input. The input images, collectively referred to by $X_{i,j}$, are first fed separately to three dilated CNNs. The architecture of the dilated CNN is shown in Fig. 5(b). It has one max-pooling layer, five regular convolutional layers and four dilated-convolutional layers with different dilation rates. The strides for all convolutional layers are 1. The two dilated CNNs that take the eyes as input share the same weights.

The feature extracted by the base CNNs are then connected to fully-connected (FC) layers, concatenated, fed to another FC layer, and finally to a linear output layer. We denote the parameters of this network by Φ .

We use Rectified Linear Units (ReLUs) as the activation functions. We apply zero-padding to regular convolutional layers, but no padding to dilated-convolutional layers. The initial weights of the first four convolutional layers are transferred from VGG-16 [50] pre-trained on the ImageNet dataset [51]. The weights in all other layers are randomly initialized. Batch renormalization layers [52] are applied to all layers trained from scratch. Dropout layers with dropout rates of 0.5 are applied to all FC layers.

3.4.1 Training

We train the network by solving the following problem by mini-batch gradient descent:

$$\min_{\Phi, \hat{b}_i} \left(\sum_{i,j} \left\| (g_{i,j} - \hat{t}(X_{i,j}; \Phi) - \hat{b}_i) \right\|_2^2 + \lambda \left\| \sum_i \hat{b}_i \right\|_1 \right), \quad (3)$$

where $\|\cdot\|_2$ represents the Euclidean norm, $\|\cdot\|_1$ represents the absolute value, and \hat{b}_i are the learned estimates of the subject-dependent bias. The second term is a regularizer that ensures that average subject-dependent bias over the training set is zero. The training is insensitive to the value of λ , since the mean bias can be compensated by \hat{t} . \hat{b}_i could also be estimated by calculating the mean for each subject over the training set, but this would be time-consuming given the large size of the training set, especially we apply online data augmentation.

We implement our network in TensorFlow. We use the Adam optimizer with default parameters. The batch size is 64. The initial learning rate is 0.001, which is divided by 10 after every ten epochs. The training proceeds for 35 epochs. We apply standard online data augmentation techniques, including random cropping, scaling, rotation and horizontal flipping. Since the bias varies if the images are horizontally flipped, we consider the non-flipped and flipped images as belonging to different subjects.

3.4.2 Testing and Calibration

During testing, gaze estimates are obtained according to Eq. (2). For a new subject m , we set $\hat{b}_m = 0$ if no calibration images are available.

A calibration set \mathcal{D}_m contains image-gaze pairs for a subject m , i.e., $\mathcal{D}_m = \{(X_{m,j}, g_{m,j}), j = 1, 2, \dots, |\mathcal{D}_m|\}$, where $|\mathcal{D}_m|$ denotes the cardinality of \mathcal{D}_m . We measure the complexity of the calibration set by the number of gaze targets T and the number of images per gaze target S . Thus, $S \cdot T = |\mathcal{D}_m|$. For best performance, the images for each gaze target should capture the variability experienced during testing, e.g. in head pose and/or illumination.

Given a calibration set \mathcal{D}_m , we set \hat{b}_m equal to the Maximum A Posteriori (MAP) estimate of the bias, assuming that $g_{m,j} - \hat{t}(X_{m,j}) \stackrel{i.i.d.}{\sim} \mathcal{N}(\hat{b}_m, \sigma_t^2 \mathbf{I})$ and that $b_m \stackrel{i.i.d.}{\sim} \mathcal{N}(\mathbf{0}, \sigma_b^2 \mathbf{I})$,

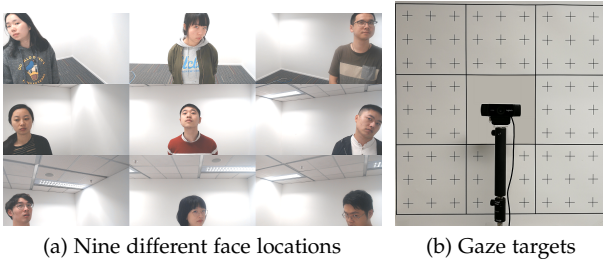


Fig. 6. The setting of dataset collection. Each subject (a) appears at nine different locations on the images and (b) is instructed to gaze at 72 crosses and the camera at each location.

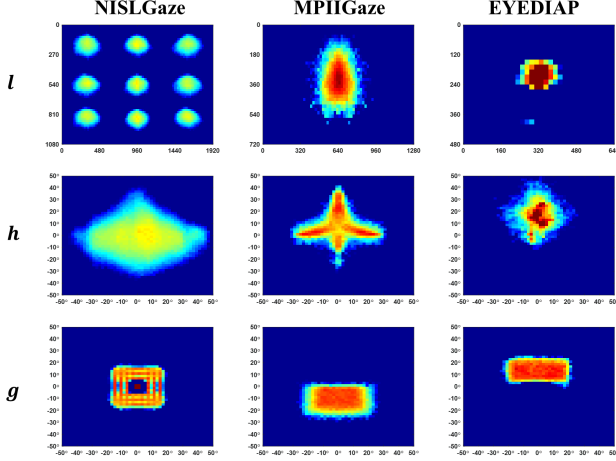


Fig. 7. Statistics of the NISLGaze (ours), MPIIGaze and EYEDIAP datasets in terms of face location (l), head pose (h) and gaze directions (g).

order. The central block was gazed at three times, while the others were gazed at only once. When the subject was asked to gaze at the central block, s/he was instructed to look at the camera; When s/he was asked to gaze at the other eight blocks, s/he was instructed to look at each of the crosses one by one. Transitions between gaze targets were signaled by a notification sound. The subject was instructed to rotate his/her head freely. We recorded one video for each gaze block, which lasted for about 30 s. This collection procedure yielded 2,079 videos (11 videos/location \times 9 locations/subject \times 21 subjects = 2,079 videos). For each subject, data collection took from one to three days. For most subjects (15), data collection spanned three days (three sessions per day).

4.2.2 Post Processing

We extracted an *Evaluation Subset* of images from the raw videos, which we used for training and testing. We first used OpenFace [49] to extract the facial landmarks and then sampled images from the video at 10 fps. We removed images for which either the landmark detector failed or both eyes were not detected. We also removed images containing blinks by setting a threshold on the eye aspect ratio calculated from the detected facial landmarks [54]. In addition, we removed images that were collected within 0.2 s after each notification sound. The resulting *Evaluation*

Subset contains 496,695 images in total (about 2,500 images for each subject at each face location).

We further defined 10 subsets of the *Evaluation Set* according to the face location. Nine of the subsets contains the images of all subjects at one face location. We denote these by *Location Subset* (α), $\alpha \in \{\text{ul, uc, ur, cl, c, cr, ll, lc, lr}\}$, where u means upper, l means lower or left depending upon whether it is in the first or second position, r means right and c means center. These nine subsets are disjoint. Their union is the *Evaluation Set*. The tenth subset is the *Mixed Location Subset*, which has a similar size as the *Location Subsets*, but contains images of all subjects at all face locations. We obtained this dataset by downsampling the *Evaluation Subset* in time by a factor of 9.

We labeled our dataset by assuming that the centers of subjects' eyes were at a fixed location in space. To be specific, we created a right-handed coordinate system whose origin was located on the wall at the center of the gaze targets with the z -axis pointing into the wall and the y -axis pointed upwards. The locations of the crosses on the wall were in the form of $(x, y, 0)$. The distance between two adjacent crosses was 6 cm. The camera was at $(0, 0, -9.5 \text{ cm})$. We assumed that the subjects' eyes were fixed at $(0, \text{height of eye} - 160 \text{ cm}, -90 \text{ cm})$. Strictly speaking, this is not true, since subjects were rotating their heads while maintaining gaze on each target. However, deviations due to this rotation were small.

5 EXPERIMENTS

We evaluated performance both with and without calibration. We evaluated on the MPIIGaze [15], the EYEDIAP [17], the ColumbiaGaze [21] and the NISLGaze datasets. We conducted both within- and cross-dataset evaluation.

We evaluated two calibration conditions: multiple gaze target calibration (MGTC) and single gaze target calibration (SGTC). For MGTC, We set the number of image per gaze target $S = 1$, but allowed the number of gaze targets T to vary. For SGTC, we set $T = 1$, but allowed S to vary. For each calibration condition, we created calibration sets by sampling from the test set. We report performance (e.g. estimation error) computed over all images in the test set, except that in the calibration set.

For ablation studies, we trained a network without dilated-convolutions using the baseline CNN shown in Fig. 5(c) and without gaze decomposition, which we refer to as **baseline CNN**. We also trained a dilated network

TABLE 1
Mean Angular Errors for Gaze Estimation without Calibration.

Name	MPIIGaze	EYEDIAP
iTracker [19]	6.2°	8.3°
iTracker (AlexNet) [14]	5.6°	
Spatial weight CNN [33]	4.8°	6.0°
CNN with shape cue [29]	4.8°	5.9°
RT-GENE [16]	4.8°	
Baseline CNN	5.3°	6.2°
Dilated CNN [25]	4.7°	5.8°
Baseline CNN + GD	4.7°	5.9°
Dilated CNN + GD	4.5°	5.4°

TABLE 2
Estimation Error (mean \pm SD in degree) of Single Gaze Target Calibration ($T = 1$) on MPIIGaze.

	Backbone	Number of images per gaze target S			
		1	5	9	16
FC	Dilated+GD	4.8 ± 0.8	7.1 ± 1.2	8.0 ± 1.2	8.4 ± 1.1
LA [41]	Dilated+GD	NA	15.1 ± 2.7	14.9 ± 2.5	14.3 ± 2.1
PA [42]	Dilated+GD	NA	NA	14.7 ± 2.4	14.3 ± 2.1
LP [36]	Dilated	4.2 ± 1.3	3.9 ± 0.8	3.8 ± 0.7	3.7 ± 0.6
DF [43]	Dilated	4.2 ± 1.5	3.5 ± 0.7	3.4 ± 0.5	3.3 ± 0.4
Baseline CNN	Baseline CNN	4.3 ± 0.9	4.0 ± 0.7	4.0 ± 0.6	3.9 ± 0.5
Dilated CNN [25]	Dilated	3.7 ± 0.9	3.4 ± 0.6	3.3 ± 0.5	3.2 ± 0.4
Dilated CNN+GD (ML) [53]	Dilated+GD	3.7 ± 1.4	3.1 ± 0.6	3.0 ± 0.4	2.9 ± 0.3
Dilated CNN+GD	Dilated+GD	3.5 ± 0.9	3.0 ± 0.5	3.0 ± 0.4	2.9 ± 0.3

TABLE 3
Estimation Error (mean \pm SD in degree) of Multiple Gaze Target Calibration ($S = 1$) on MPIIGaze.

Face+Eye	Backbone	Number of gaze targets T						
		1	5	9	16	32	64	128
FC	Dilated+GD	4.8 ± 0.8	5.5 ± 1.5	4.5 ± 1.0	3.5 ± 0.5	2.9 ± 0.2	2.7 ± 0.1	2.5 ± 0.1
LA [41]	Dilated+GD	NA	4.7 ± 3.0	3.1 ± 0.7	2.8 ± 0.3	2.6 ± 0.1	2.5 ± 0.1	2.4 ± 0.0
PA [42]	Dilated+GD	NA	NA	9.2 ± 3.5	3.8 ± 1.3	2.8 ± 0.3	2.6 ± 0.1	2.4 ± 0.0
LP [36]	Dilated	4.2 ± 1.3	3.3 ± 0.4	3.2 ± 0.3	3.0 ± 0.1	3.0 ± 0.1	2.9 ± 0.1	2.9 ± 0.0
DF [43]	Dilated	4.2 ± 1.5	3.2 ± 0.4	3.0 ± 0.3	3.0 ± 0.1	2.6 ± 0.1	2.6 ± 0.0	2.6 ± 0.0
Baseline CNN	Baseline CNN	4.3 ± 0.9	3.6 ± 0.5	3.5 ± 0.4	3.4 ± 0.3	3.4 ± 0.1	3.3 ± 0.0	3.3 ± 0.0
Dilated CNN [25]	Dilated	3.7 ± 0.9	3.1 ± 0.4	3.0 ± 0.2	2.9 ± 0.2	2.9 ± 0.1	2.9 ± 0.0	2.9 ± 0.0
Dilated CNN+GD (ML) [53]	Dilated+GD	3.7 ± 1.4	2.9 ± 0.4	2.7 ± 0.2	2.7 ± 0.1	2.6 ± 0.1	2.6 ± 0.0	2.6 ± 0.0
Dilated CNN+GD	Dilated+GD	3.5 ± 0.9	2.8 ± 0.4	2.7 ± 0.2	2.7 ± 0.1	2.6 ± 0.1	2.6 ± 0.0	2.6 ± 0.0
Eye only								
GRS [44]*	VGG16	5.0	4.2	4.0				
FAZE [45]*	DenseNet	4.7	4.0	3.9	3.8	3.8	3.7	3.7
Dilated CNN+GD*	Dilated+GD	4.1 ± 0.9	3.5 ± 0.4	3.4 ± 0.3	3.3 ± 0.3	3.3 ± 0.1	3.3 ± 0.0	3.3 ± 0.0

*: The three methods at the bottom only used eye images as input, while the others used face+eye images as input.

without gaze decomposition, **dilated CNN**, and a baseline CNN with gaze decomposition, **baseline CNN+GD**. Our proposed method is denoted by **dilated CNN+GD**.

5.1 Results on MPIIGaze, EYEDIAP and Columbia

5.1.1 Within-Dataset Evaluation

Gaze Estimation without Calibration. For the MPIIGaze dataset, we conducted 15-fold leave-one-subject-out cross-validation. For the EYEDIAP dataset, we followed the protocol described in [33], namely, five-fold cross-validation on four VGA videos (both continuous and discrete screen targets with both static and dynamic head pose) sampled at 2 fps, resulting in about 1,200 images per subject.

We compared our method with several baselines: iTracker [19], [33], spatial weights CNN [33], CNN with shape cue [29], RT-GENE without ensembling [16] and Dilated-Net [25]. All of these methods used face images (or face plus eye images) as input. We re-implemented the CNN with shape cue and used the originally published results for the other methods.

The results are shown in TABLE 1. On MPIIGaze, our proposed network achieved a 4.5° mean angular error, outperforming the state-of-the-art 4.8° [16], [25], [29], [33]

by 6.3%. On EYEDIAP, it achieved 5.4° , outperforming the state-of-the-art 5.9° [29] by 8.5%.

Calibration Procedures. For MGTC, T images from the test set were randomly selected as \mathcal{D}_m . For SGTC, we first randomly selected a calibration target in the 2D (yaw, pitch) gaze space. We then randomly selected S images whose true gaze angles differed from the calibration target by less than 2° as \mathcal{D}_m . We discarded the gaze target if fewer than S images met the 2° requirement. After calibration, testing was conducted on the images not belonging to \mathcal{D}_m .

We also calculated the estimation error achieved by estimating the bias of each subject from all images in the test set and evaluating on the test set. This serves as a lower bound of our methods, and is denoted by \underline{E} . We denote the mean angular error without calibration by \bar{E} .

Calibration Results. We compared the estimation error of our approach with that of other existing calibration methods: fine-tuning the last FC layer (FC), linear adaptation (LA) [41], third order polynomial adaptation (PA) [42], the differential method (DF) [43], fine-tuning the latent parameters (LP) [36], gaze redirection synthesis

(GRS) [44] and FAZE [45]. FC, LA and PA were applied to our network trained with gaze decomposition. DF and LP were re-implemented in a network with the same architecture as in Fig. 5. For GRS and FAZE, we used their originally published results in the same within-dataset leave-one-subject-out cross-validation. Since both GRS and FAZE only considered eye images as input, we trained a network without the face component in Fig. 5 for fair comparison.

The results are shown in Tables 2 and 3, where the estimation errors reported were averaged over all subjects and over 5,000 calibration iterations per subject. For all methods, as the complexity of the calibration set increases (the number of calibration gaze targets and/or the number of images increases), the error decreases. Our proposed method performed the best for low complexity calibration sets, outperforming other methods for all tested cases of SGTC and for MGTC when the number of images was less than or equal to 16. For example, for SGTC with 9 samples, our proposed algorithm reduced the error by 11.8% compared to the second best method (DF). We attribute this better performance to that our approach use small number of parameters for calibration, which avoids overfitting. Unlike LP, our approach directly rectifies the final output of a subject-independent gaze estimator. This reduces the error significantly, as the primary cause of error is a subject-dependent bias. Given enough calibration data, other methods like LA and PA eventually outperform ours. However, this does not happen until the number of gaze target is more than 32, which will be too time-consuming for most real-world applications. For example, most commercial eye trackers usually use nine gaze targets for calibration. This is often reduced to five to save time at the expense of poorer calibrations.

The MAP estimate of the bias described in Eq. (4) resulted in lower estimation error than the ML estimate we proposed previously in [53], especially when $|\mathcal{D}_m|$ was small. For example, with only one calibration image, the error when using the proposed MAP estimate was 3.5, 0.2° (5.4%) lower than the 3.7° achieved by the ML estimate.

For our proposed calibration method, SGTC reduced estimation error significantly. When calibrated on 9 samples, it reduced the error by 1.5° (33.3%) in comparison to the estimator without calibration. MGTC led to further reductions, but on average SGTC achieved 90% of the improvement achieved by MGTC using the same number of images.

To evaluate the robustness of SGTC to the location of calibration target, we evaluated the performance when the calibration target was located in 24 different $5^\circ \times 5^\circ$ regions. We set $S = 9$, since the error reduction from our above experiment saturated beyond this point. Fig. 8 shows the results. The error achieved when the calibration target is at the center of the gaze range was lower than the error when the gaze target was located at the boundary. However, the standard deviation over regions was only 0.16° , indicating that SGTC is quite robust to the location of calibration target.

Our experimental results on the EYEDIAP dataset were consistent with those presented above on the MPIIGaze dataset. We include the results and detailed analysis in Appendix A.

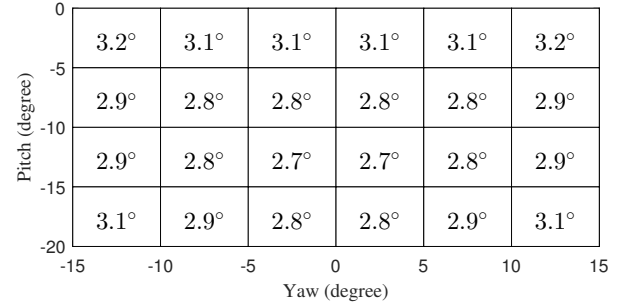


Fig. 8. The mean angular error on MPIIGaze for SGTC ($S = 9$). The number in each box shows the mean angular error when the calibration gaze target is located inside the corresponding 5×5 region. Mean errors are computed by averaging over the entire test set (except for the calibration set) and over 100 calibration gaze targets located at a 10×10 grid spaced by 0.5° in yaw and pitch inside each region. $\bar{E} = 4.5^\circ$, $\underline{E} = 2.6^\circ$.

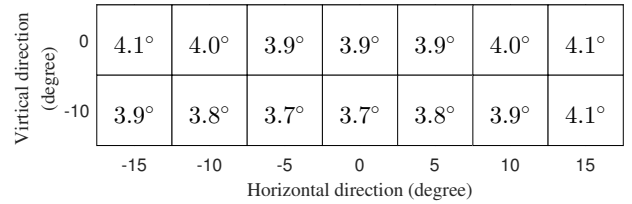


Fig. 9. Cross-dataset evaluation. Mean angular error of SGTC ($S = 5$) when calibrated at different gaze targets. Trained on MPIIGaze and NISLGaze. Tested on the ColumbiaGaze. $\bar{E} = 4.8^\circ$, $\underline{E} = 3.6^\circ$.

5.1.2 Cross-Dataset Evaluation

We trained our network on the MPIIGaze and the NISLGaze datasets combined, and tested it on the ColumbiaGaze dataset. We excluded the images corresponding to 10° vertical angle from the ColumbiaGaze dataset for these evaluations, since the MPIIGaze dataset mainly covers pitch angles from -20° to 0° .

Fig. 9 shows the error of SGTC when calibrating at different gaze targets, where we used the five images gazing at the same gaze target but with different head poses as the calibration set ($S = 5$, $T = 1$). The error ranged from 3.7° to 4.1° , which was 14.6% to 22.9% lower than without calibration ($\bar{E} = 4.8^\circ$).

We also compared our method with LP and DF as these two methods performed well for SGTC from previous results. The results are presented in Table 4. Our proposed algorithm performed the best, outperforming DF by 0.3° (7.1%) and LP by 1.2° (23.5%).

TABLE 4
Cross-Dataset of SGTC on ColumbiaGaze ($T = 1$, $S = 5$)

Training set	Method	Error
MPIIGaze and NISLGaze (Location Subset(c))	LP [36]	5.1°
	DF [43]	4.2°
	Baseline CNN	4.4°
	Dilated + GD	3.9°

TABLE 5
Estimation Error on NISLGaze under Different Training Sets and Calibration Methods

Calibration \ Training set	Multiple Location			Center Location		
	Overall	Center	Periphery	Overall	Center	Periphery
Without Calibration	$4.53^\circ \pm 0.09^\circ$	4.55°	$4.53^\circ \pm 0.09^\circ$	$4.61^\circ \pm 0.14^\circ$	4.44°	$4.64^\circ \pm 0.13^\circ$
Center location calibration	$3.28^\circ \pm 0.11^\circ$	3.18°	$3.29^\circ \pm 0.11^\circ$	$3.51^\circ \pm 0.20^\circ$	3.18°	$3.55^\circ \pm 0.16^\circ$
Matched location calibration	$3.27^\circ \pm 0.11^\circ$	3.18°	$3.28^\circ \pm 0.11^\circ$	$3.52^\circ \pm 0.21^\circ$	3.18°	$3.57^\circ \pm 0.18^\circ$

Each entry presents mean \pm SD, where SD is computed over face locations. **Overall**: the average estimation error over test samples from all nine face locations. **Center**: the estimation error on test samples when the face is at the center location. **Periphery**: the average estimation error over test samples from the eight face locations excluding the center.

5.1.3 Ablation Studies

We performed ablation studies to determine how much of the improvement in performance was due to the use of dilated-convolutions and how much was due to the use of gaze decomposition. Table 1 shows that applying dilated-convolutions without gaze decomposition reduced estimation error by 0.6° (11.3%) on MPIIGaze and by 0.4° (6.5%) on EYEDIAP when compared to the Baseline CNN without gaze decomposition. Applying gaze decomposition to the Baseline CNN resulted in a similar improvement, 0.6° (11.3%) on MPIIGaze and 0.3° (4.8%) on EYEDIAP. Applying both dilated-convolutions and gaze decomposition achieved the best performance, reducing the error by 0.8° (15.1%) on MPIIGaze and by 0.8° (12.9%) on EYEDIAP compared to Baseline CNN.

Similar improvements were observed with calibration. For example, the Dilated CNN without gaze decomposition outperformed the Baseline CNN without decomposition by 0.6° to 0.7° with SGTC (Table 2) and by 0.4° to 0.6° with MGTC (Table 3). Applying gaze decomposition to the Dilated CNN reduced error further by 0.2° to 0.4° for SGTC (Table 2) and by 0.2° to 0.3° for MGTC.

5.2 Results on NISLGaze

We used the NISLGaze dataset to examine the robustness to changes of the face location in the image. In previously collected datasets, the subject’s face is mainly in the center of the image. However, one of the primary potential advantage of appearance-based gaze estimators is that they may allow for less constrained head movements (rotation and translation) than active illumination based approaches, but to the best of our knowledge this has never been systematically evaluated before.

Training and Testing. We trained two networks, which differed by their training data. The first network was trained on a “Multiple Location” dataset formed by the union of the MPIIGaze, the EYEDIAP and the NISLGaze (*Mixed Location Subset*) datasets. The second network was trained on a “Center Location” dataset formed by the union of the MPIIGaze, the EYEDIAP and the NISLGaze (*Location Subset (c)*) datasets. See Section 4.2.2 for the definition of these subsets. The two datasets differed in the diversity of locations where the face appeared in the image. The first has a greater diversity than the second. For the MPIIGaze and EYEDIAP datasets, most faces appear in the center of

the image. The face location diversity depended primarily on the NISLGaze data subset included.

For evaluation, we conducted five-fold inter-subject cross-validation, where we split the folds by subject. Four folds contained the data from four subjects. The fifth contained data from five (21 subjects total). All training was performed with gaze decomposition. All testing was performed on the data from *Evaluation Subset*.

Calibration. We considered two types of calibration. In **center location calibration**, calibration was conducted on the data with the face in the center of the image, but the estimator was tested with the face in all locations. In **matched location calibration**, the face was in the same location in both calibration and testing data. In the first case, calibration was performed once per trial and then the estimator was tested at all nine locations. In the second case, calibration and testing was performed nine times per trial, once for each face location. In each trial, the calibration data was obtained by taking 16 consecutive frames sampled at 10 fps with the subject gazing only at the camera, but moving his/her head, i.e., SGTC. Calibration data was excluded from the testing data. Estimation error was averaged over 500 trials and over all subjects from all folds.

Center location calibration is a more realistic setting, where calibration is performed only once and tested at different face locations. We were interested in evaluating matched location calibration to see if the mismatch between the calibration and testing locations of the face would degrade accuracy.

We used only calibration data taken as the subject gazed at the camera, because we felt that this is an interesting use case for SGTC, since the camera will always be visible to the subject and it may not always be possible or convenient to divert the subject’s gaze towards other known points in the environment. Using consecutive frames makes this experiment a better reflection of the situation we expect in real world situations.

5.2.1 Results of Gaze Estimation

Table 5 shows estimation error of the two networks trained on different training sets. For both networks, applying calibration significantly reduced the estimation error. For example, for the network trained at multiple locations, center location calibration reduced the estimation error by 1.3° (28.9%) compared to the 4.5° achieved without calibration.

Interestingly, we did not observe any difference of estimation error between center location calibration and matched location calibration for either of the two networks. This suggests that for calibration, the offset caused by mismatch between the calibration and testing location is negligible. To further validate this, we calculated the bias for each subject and for each face location by averaging the gaze estimate from all images taken as the subject gazed at the camera from that location, for the network trained on mixed locations. We observed wide variation in the means from subject to subject (from -2.7° to 3.4° in yaw and from -7.5° to 5.6° in pitch), but very little variations across locations for each subject (SDs ranged from 0.1° to 0.5° for yaw and from 0.2° to 0.7° for pitch). A repeated measures analysis of variance (ANOVA) did not indicate a statistically significant effect of the face location on the value of biases (yaw $F(8, 160) = 1.63, p = .12$; pitch $F(8, 160) = 1.48, p = .17$). These results indicate that the biases estimated at different face locations are similar for the same subject. In other words, the bias estimated from the central face location can be applied to different face locations, which is a significant advantage in real-world applications.

We also evaluated the effect of increasing the diversity of face locations in the training set. Unlike the effect of the face location on calibration, where we found no effect, here we did discover an effect. Table 5 shows that when trained only on data with the face at the center location, the estimation error at the periphery increased by 12% compared to the center.

When trained with the face at multiple locations, we observe a 7% decrease in the estimation error at the periphery and no change at the center, compared to trained with the face only at the center. Overall error averaged over all locations decreased by 7% as well. The performance drop at periphery is not fully eliminated, which may partly because the image normalization method [47] can not fully cancel out all of the distortions introduced when the face appears at the periphery rather than the center.

Thus, training with the face at multiple locations improves performance, but calibration with the face at one location transfers to other locations. This suggests that the bias observed between subject is partly due to intrinsic factors, such as the difference between the optic and visual axes, rather than extrinsic factors like appearance difference caused by face location.

5.2.2 Comparison to Other Methods

We compared with LP and DF, which were the best two competing methods for SGTC (Table 2). Table 6 shows the results when trained on the ‘‘Multiple Location’’ dataset

TABLE 6
Single Gaze Target Calibration on NISLGaze ($T = 1, S = 16$) by
Matched Location Calibration.

Training set	Method	Error
MPIIGaze +	LP [36]	4.4°
EYEDIAP +	DF [43]	3.7°
NISLGaze	Baseline CNN	3.7°
(Mixed Location Subset)	Dilated + GD	3.3°

and testing with matched location calibration. Our method outperformed DF by 0.4° (10.8%) and LP by 1.1° (25.0%).

6 ANALYSIS

The results of the ablation studies in Table 1, 2 and 3 and described in Section 5.1.3 showed that both the adoption of dilated-convolutions in the network architecture and the use of the gaze decomposition in training improved test performance both with and without calibration. We attribute the improvement due to dilated-convolutions to an improvement in the structure of the subject-independent component of the gaze estimator, i.e., $\hat{t}(X_{i,j}; \Phi)$ in Eq. (2). Thus, the increment in performance both with and without calibration was not surprising. We were also not surprised by the improvement in test performance with calibration when the network was trained with gaze composition, since it makes sense to model the effect of the additive bias during training.

However, we were surprised to see an improvement in test performance *without* calibration when the estimator was trained *with* gaze decomposition, since the train and test conditions are mismatched: additive bias during training but no additive bias during testing.

To give a theoretical insight into why and under what conditions this might be expected, we analyzed a linear Gaussian model of image formation. Although the actual image formation process is more complex and highly nonlinear, this analysis is analytically tractable and provides insight into the performance of estimators trained with/without gaze decomposition when tested with/without calibration.

In our model, we define $X_{i,j} \in \mathbb{R}^s$ to be the j^{th} image of the i^{th} subject, where j ranges from 1 to J (the total number of images per subject) and i ranges from 1 to I (the total number of subjects). We model the image formation process by

$$X_{i,j} = W_t t_{i,j} + W_c c_i + v_{i,j}, \quad (5)$$

$$g_{i,j} = t_{i,j} + b_i \quad (6)$$

where $t_{i,j} \in \mathbb{R}^2$ is the direction of the optic axis, $c_i \in \mathbb{R}^p$ captures subject-dependent variations in appearance, $v_{i,j} \in \mathbb{R}^s$ is a noise term, $g_{i,j} \in \mathbb{R}^2$ is the direction of the visual axis (the gaze direction) and $b_i \in \mathbb{R}^2$ is a subject-dependent difference between the visual and optical axes. We assume that $s \geq 2 + p$ and that both $W_t \in \mathbb{R}^{s \times 2}$ and $W_c \in \mathbb{R}^{s \times p}$ have full column rank. We assume that $t_{i,j}$, c_i , $v_{i,j}$, b_i are zero-mean Gaussian random variables whose covariance matrices are denoted by Σ_t , Σ_c , Σ_v and Σ_b , and that random variables with different values of i and j are independent.

Let

$$\hat{g}_{i,j} = \mathcal{K} X_{i,j} \quad (7)$$

be a linear subject-independent estimator of the gaze direction $g_{i,j}$ from an image $X_{i,j}$ where $\mathcal{K} \in \mathbb{R}^{2 \times s}$ and the hat indicates the quantity is an estimate. For convenience, we will refer to a subject-independent estimator using its \mathcal{K} matrix.

We define the mean squared error without calibration to be

$$\text{MSE}_{\text{cal}}(\mathcal{K}) = \text{tr} \left\{ \mathbb{E} \left[(g_{i,j} - \mathcal{K} X_{i,j})(g_{i,j} - \mathcal{K} X_{i,j})^\top \right] \right\}, \quad (8)$$

where $E[\cdot]$ is the expected value, tr is the matrix trace operator and \top indicates transpose. Since the model is linear and all random variables are Gaussian and zero mean, the optimal estimator without calibration is [55]

$$\mathcal{K}_{\text{cal}} = \Sigma_{gX} \Sigma_X^{-1} \quad (9)$$

where

$$\Sigma_{gX} = E[g_{i,j} X_{i,j}^\top] \quad (10)$$

$$= \Sigma_t W_t^\top, \quad (11)$$

$$\Sigma_X = E[X_{i,j} X_{i,j}^\top] \quad (12)$$

$$= W_t \Sigma_t W_t^\top + W_c \Sigma_c W_c^\top + \Sigma_v. \quad (13)$$

In an ideal case where the subject-dependent terms, c_i and b_i are known, we can calibrate the estimator by adding a subject dependent bias

$$\hat{g}_{i,j} = \mathcal{K} X_{i,j} + \mu_i, \quad (14)$$

where

$$\mu_i = b_i - \mathcal{K} W_c c_i. \quad (15)$$

We define the mean squared error with ideal calibration to be

$$\text{MSE}_{\text{cal}}(\mathcal{K}) = \text{tr} \left\{ E \left[(g_{i,j} - (\mathcal{K} X_{i,j} + \mu_i)) \times (g_{i,j} - (\mathcal{K} X_{i,j} + \mu_i))^\top \right] \right\}. \quad (16)$$

The optimal estimator with ideal calibration is

$$\mathcal{K}_{\text{cal}} = C_{gX} C_X^{-1}, \quad (17)$$

where

$$C_{gX} = E[(g_{i,j} - b_i)(X_{i,j} - W_c c_i)^\top] \quad (18)$$

$$= \Sigma_t W_t^\top, \quad (19)$$

$$C_X = E[(X_{i,j} - W_c c_i)(X_{i,j} - W_c c_i)^\top] \quad (20)$$

$$= W_t \Sigma_t W_t^\top + \Sigma_v \quad (21)$$

are covariance matrices where the data is centered by subject dependent offsets. The difference between the case without calibration and the case with calibration is that without calibration both c_i and $v_{i,j}$ are considered noise terms added to the image, but with ideal calibration, only $v_{i,j}$ is considered a noise term.

In practice, the constants W_t , W_c , Σ_t , Σ_c and Σ_v are not known. Estimates of the matrices \mathcal{K}_{cal} and \mathcal{K}_{cal} must be estimated from training data. Nor are the random variables b_i and c_i known. Rather, an estimate of the bias must be obtained from user calibration data.

Assume a set of training data, $\mathcal{D}_{\text{tr}} = \{(X_{i,j}, g_{i,j}) \mid i = 1, 2, \dots, I_{\text{tr}}, j = 1, 2, \dots, J_{\text{tr}}\}$. For an estimator $\hat{\mathcal{K}}$, we define the empirical mean squared error *without* gaze decomposition by

$$\widehat{\text{MSE}}_{\text{dec}}(\hat{\mathcal{K}}) = \text{tr} \left\{ \hat{E} \left[(g_{i,j} - \hat{\mathcal{K}} X_{i,j})(g_{i,j} - \hat{\mathcal{K}} X_{i,j})^\top \right] \right\} \quad (22)$$

where $\hat{E}[\cdot]$ is the empirical expected value:

$$\hat{E}[A_{i,j}] = \frac{1}{IJ} \sum_{i=1}^I \sum_{j=1}^J A_{i,j}. \quad (23)$$

This is an empirical estimate of the mean squared error without calibration. We use the hat to indicate empirical estimates. The optimal estimator that minimizes $\widehat{\text{MSE}}_{\text{dec}}$ is given by

$$\hat{\mathcal{K}}_{\text{dec}} = \hat{\Sigma}_{gX} \hat{\Sigma}_X^{-1}, \quad (24)$$

where

$$\hat{\Sigma}_{gX} = \hat{E}[g_{i,j} X_{i,j}^\top], \quad (25)$$

$$\hat{\Sigma}_X = \hat{E}[X_{i,j} X_{i,j}^\top]. \quad (26)$$

By the law of large numbers, $\hat{\mathcal{K}}_{\text{dec}} \rightarrow \mathcal{K}_{\text{cal}}$ when $I_{\text{tr}}, J_{\text{tr}} \rightarrow \infty$.

For an estimator $\hat{\mathcal{K}}$ and a set of subject dependent biases $\{\hat{\mu}_i\}_{i=1}^{I_{\text{tr}}}$, we define the empirical mean squared error *with* gaze decomposition

$$\widehat{\text{MSE}}_{\text{dec}}(\hat{\mathcal{K}}, \{\hat{\mu}_i\}) = \text{tr} \left\{ \hat{E} \left[(g_{i,j} - (\hat{\mathcal{K}} X_{i,j} + \hat{\mu}_i)) \times (g_{i,j} - (\hat{\mathcal{K}} X_{i,j} + \hat{\mu}_i))^\top \right] \right\}. \quad (27)$$

For the optimal set of biases, this is an empirical estimate of the mean squared error with ideal calibration. The optimal empirical estimator and set of biases that minimize $\widehat{\text{MSE}}_{\text{dec}}$ are given by

$$\hat{\mathcal{K}}_{\text{dec}} = \hat{C}_{gX} \hat{C}_X^{-1}, \quad (28)$$

$$\hat{\mu}_i = \hat{E}_j[g_{i,j}] - \hat{\mathcal{K}}_{\text{dec}} \hat{E}_j[X_{i,j}], \quad (29)$$

where

$$\hat{C}_{gX} = \hat{E}[(g_{i,j} - \hat{E}_j[g_{i,j}])(X_{i,j} - \hat{E}_j[X_{i,j}])^\top] \quad (30)$$

$$= \hat{E}[g_{i,j} X_{i,j}^\top] - \hat{E}_i[\hat{E}_j[g_{i,j}]] \hat{E}_j[X_{i,j}^\top], \quad (31)$$

$$\hat{C}_X = \hat{E}[(X_{i,j} - \hat{E}_j[X_{i,j}])(X_{i,j} - \hat{E}_j[X_{i,j}])^\top] \quad (32)$$

$$= \hat{E}[X_{i,j} X_{i,j}^\top] - \hat{E}_i[\hat{E}_j[X_{i,j}]] \hat{E}_j[X_{i,j}^\top], \quad (33)$$

and we define the empirical mean operators

$$\hat{E}_i[A_{i,j}] = \frac{1}{I} \sum_{i=1}^I A_{i,j} \text{ and } \hat{E}_j[A_{i,j}] = \frac{1}{J} \sum_{j=1}^J A_{i,j}. \quad (34)$$

The terms $\hat{E}_j[g_{i,j}]$ and $\hat{E}_j[X_{i,j}]$ can be considered to be empirical estimates of b_i and $W_c c_i$, respectively. By the law of large numbers, $\hat{\mathcal{K}}_{\text{dec}} \rightarrow \mathcal{K}_{\text{cal}}$ and $\hat{\mu}_i \rightarrow \mu_i$ as $I_{\text{tr}}, J_{\text{tr}} \rightarrow \infty$.

By optimality, it must be true that

$$\text{MSE}_{\text{cal}}(\mathcal{K}_{\text{cal}}) \leq \text{MSE}_{\text{cal}}(\hat{\mathcal{K}}_{\text{cal}}) \quad (35)$$

and

$$\text{MSE}_{\text{cal}}(\mathcal{K}_{\text{cal}}) \leq \text{MSE}_{\text{cal}}(\mathcal{K}_{\text{cal}}). \quad (36)$$

Thus, by the law of large numbers,

$$\lim_{I_{\text{tr}}, J_{\text{tr}} \rightarrow \infty} \text{MSE}_{\text{cal}}(\hat{\mathcal{K}}_{\text{dec}}) \leq \lim_{I_{\text{tr}}, J_{\text{tr}} \rightarrow \infty} \text{MSE}_{\text{cal}}(\hat{\mathcal{K}}_{\text{dec}}) \quad (37)$$

and

$$\lim_{I_{\text{tr}}, J_{\text{tr}} \rightarrow \infty} \text{MSE}_{\text{cal}}(\hat{\mathcal{K}}_{\text{dec}}) \leq \lim_{I_{\text{tr}}, J_{\text{tr}} \rightarrow \infty} \text{MSE}_{\text{cal}}(\hat{\mathcal{K}}_{\text{dec}}). \quad (38)$$

The second equation is consistent with our experimental results, where we observe an improvement in test performance with calibration when the network is trained with gaze decomposition. However, at first glance, it appears that

the first equation is not, since we observe better test performance without calibration when the network is trained with gaze decomposition.

The remainder of this section will discuss how to resolve this apparent contradiction. Briefly, we prove that if variations in appearance due to gaze and due to subject are orthogonal ($W_t^\top W_c = \mathbf{0}$), then the optimal estimators without calibration and with ideal calibration are identical, i.e. $\mathcal{K}_{\text{cal}} = \mathcal{K}_{\text{cal}}$ (Theorem 1). Thus,

$$\text{MSE}_{\text{cal}}(\mathcal{K}_{\text{cal}}) = \text{MSE}_{\text{cal}}(\mathcal{K}_{\text{cal}}) \quad (39)$$

and

$$\lim_{I_{\text{tr}}, J_{\text{tr}} \rightarrow \infty} \text{MSE}_{\text{cal}}(\hat{\mathcal{K}}_{\text{dec}}) = \lim_{I_{\text{tr}}, J_{\text{tr}} \rightarrow \infty} \text{MSE}_{\text{cal}}(\hat{\mathcal{K}}_{\text{dec}}). \quad (40)$$

Moreover, we prove that for any finite number of subjects I_{tr} and as the number of (gaze, image) pairs per subject J_{tr} approaches infinity, the gaze estimator trained with gaze decomposition performs *as well as or better* than the gaze estimator trained without gaze decomposition. In other words, the direction of the inequality in Eq. (37) is reversed (Theorem 2):

$$\lim_{J_{\text{tr}} \rightarrow \infty} \text{MSE}_{\text{cal}}(\hat{\mathcal{K}}_{\text{dec}}) \geq \lim_{J_{\text{tr}} \rightarrow \infty} \text{MSE}_{\text{cal}}(\hat{\mathcal{K}}_{\text{dec}}). \quad (41)$$

In the case where the variations in appearance and gaze are not orthogonal ($W_t^\top W_c \neq \mathbf{0}$), then the inequalities in Eqs. (35) and (37) are strict. Nonetheless, our numerical results with this model still show that if the sizes of $W_t^\top W_c$ and I_{tr} are small enough, then the inequality Eq. (41) still holds. These results resolve the apparent contradiction with our experimental results raised above, by suggesting that in practice the variations in appearance due to gaze and due to subject are close to orthogonal.

The following theorem shows that under certain conditions \mathcal{K}_{cal} and \mathcal{K}_{cal} are identical.

Theorem 1. *If $W_t^\top W_c = \mathbf{0}$ and the elements of the noise vector $v_{i,j}$ are independent and identically distributed, i.e., $\Sigma_v = \sigma_v^2 \mathbf{I}_k$, then $\mathcal{K}_{\text{cal}} = \mathcal{K}_{\text{cal}}$.*

Proof. Combining Eq. (13) with $\Sigma_v = \sigma_v^2 \mathbf{I}_k$ and the definitions $U = [W_t \ W_c]$ and

$$\Sigma = \begin{bmatrix} \sigma_v^{-2} \Sigma_t & \mathbf{0} \\ \mathbf{0} & \sigma_v^{-2} \Sigma_c \end{bmatrix}, \quad (42)$$

we can write $\Sigma_X^{-1} = \sigma_v^{-2} (\mathbf{I} + U \Sigma U^\top)^{-1}$. Using the Woodbury matrix identity [56],

$$\Sigma_X^{-1} = \sigma_v^{-2} (\mathbf{I} - U (\Sigma^{-1} + U^\top U)^{-1} U^\top). \quad (43)$$

Since $W_t^\top W_c = \mathbf{0}$,

$$\begin{aligned} & (\Sigma^{-1} + U^\top U)^{-1} \\ &= \left(\begin{bmatrix} \sigma_v^2 \Sigma_t^{-1} & \mathbf{0} \\ \mathbf{0} & \sigma_v^2 \Sigma_c^{-1} \end{bmatrix} + \begin{bmatrix} W_t^\top \\ W_c^\top \end{bmatrix} [W_t \ W_c] \right)^{-1} \end{aligned} \quad (44)$$

$$= \begin{bmatrix} \sigma_v^2 \Sigma_t^{-1} + W_t^\top W_t & \mathbf{0} \\ \mathbf{0} & \sigma_v^2 \Sigma_c^{-1} + W_c^\top W_c \end{bmatrix}^{-1}. \quad (45)$$

Substituting into Eq. (43),

$$\begin{aligned} \Sigma_X^{-1} &= \sigma_v^{-2} \left(\mathbf{I} - W_t (\sigma_v^2 \Sigma_t^{-1} + W_t^\top W_t)^{-1} W_t^\top \right. \\ &\quad \left. - W_c (\sigma_v^2 \Sigma_c^{-1} + W_c^\top W_c)^{-1} W_c^\top \right). \end{aligned} \quad (46)$$

Substituting into Eq. (9) and using $W_t^\top W_c = \mathbf{0}$, we obtain

$$\mathcal{K}_{\text{cal}} = \Sigma_t W_t^\top \left(\sigma_v^{-2} [\mathbf{I} - W_t (\sigma_v^2 \Sigma_t^{-1} + W_t^\top W_t)^{-1} W_t^\top] \right) \quad (47)$$

$$= \Sigma_t W_t^\top (\Sigma_v + W_t \Sigma_t W_t^\top)^{-1} \quad (48)$$

$$= \mathcal{K}_{\text{cal}}. \quad (49)$$

The equivalence between the first and second lines can be obtained by the Woodbury matrix identity. \square

The first line of the proof can be manipulated to show that both \mathcal{K}_{cal} and \mathcal{K}_{cal} can be written as

$$\sigma_v^{-2} \Sigma_t \left[\mathbf{I} - W_t^\top W_t (\sigma_v^2 \Sigma_t^{-1} + W_t^\top W_t)^{-1} \right] W_t^\top. \quad (50)$$

If $W_t^\top W_c = \mathbf{0}$, then $\mathcal{K}_{\text{cal}} W_c = \mathcal{K}_{\text{cal}} W_c = \mathbf{0}$. In other words, the ideal estimators are insensitive to the subject dependent changes in appearance.

Theorem 2. *Let \mathcal{D}_{tr} be an arbitrary training set with I_{tr} subjects and J_{tr} samples per subject. If $W_t^\top W_c = \mathbf{0}$ and $\Sigma_v = \sigma_v^2 \mathbf{I}_k$, then*

$$\lim_{J_{\text{tr}} \rightarrow \infty} \text{MSE}_{\text{cal}}(\hat{\mathcal{K}}_{\text{dec}}) \geq \lim_{J_{\text{tr}} \rightarrow \infty} \text{MSE}_{\text{cal}}(\hat{\mathcal{K}}_{\text{dec}}).$$

Proof. Since $\hat{E}[A_{i,j}] = \hat{E}_i[\hat{E}_j[A_{i,j}]]$ using (5) and (6), we have by the law of large numbers that

$$\hat{E}[g_{i,j} X_{i,j}^\top] \xrightarrow{J_{\text{tr}} \rightarrow \infty} \Sigma_t W_t^\top + \hat{E}_i[b_i c_i^\top] W_c^\top, \quad (51)$$

$$\hat{E}[X_{i,j} X_{i,j}^\top] \xrightarrow{J_{\text{tr}} \rightarrow \infty} W_t \Sigma_t W_t^\top + W_c \hat{\Sigma}_c W_c^\top + \Sigma_v, \quad (52)$$

and that

$$\hat{E}_i[\hat{E}_j[g_{i,j}] \hat{E}_j[X_{i,j}^\top]] \xrightarrow{J_{\text{tr}} \rightarrow \infty} \hat{E}_i[b_i c_i^\top] W_c^\top, \quad (53)$$

$$\hat{E}_i[\hat{E}_j[X_{i,j}] \hat{E}_j[X_{i,j}^\top]] \xrightarrow{J_{\text{tr}} \rightarrow \infty} W_c \hat{\Sigma}_c W_c^\top, \quad (54)$$

where $\hat{\Sigma}_c = \hat{E}_i[c_i c_i^\top]$.

Substituting Eqs. (51)-(54) into Eqs. (24)-(26) and using the Woodbury matrix identity and $W_t^\top W_c = \mathbf{0}$,

$$\begin{aligned} \hat{\mathcal{K}}_{\text{dec}} &\xrightarrow{J_{\text{tr}} \rightarrow \infty} (\Sigma_t W_t^\top + \hat{E}_i[b_i c_i^\top] W_c^\top) \\ &\quad \times (W_t \Sigma_t W_t^\top + W_c \hat{\Sigma}_c W_c^\top + \Sigma_v)^{-1} \end{aligned} \quad (55)$$

$$\begin{aligned} &= (\Sigma_t W_t^\top + \hat{E}_i[b_i c_i^\top] W_c^\top) \sigma_v^{-2} \\ &\quad \times \left(\mathbf{I} - W_t (\sigma_v^2 \Sigma_t^{-1} + W_t^\top W_t)^{-1} W_t^\top \right. \\ &\quad \left. - W_c (\sigma_v^2 \hat{\Sigma}_c^{-1} + W_c^\top W_c)^{-1} W_c^\top \right) \end{aligned} \quad (56)$$

$$\begin{aligned} &= \sigma_v^{-2} \left(\Sigma_t W_t^\top + \hat{E}_i[b_i c_i^\top] W_c^\top \right. \\ &\quad \left. - \Sigma_t W_t^\top W_t (\sigma_v^2 \Sigma_t^{-1} + W_t^\top W_t)^{-1} W_t^\top \right. \\ &\quad \left. - \hat{E}_i[b_i c_i^\top] W_c^\top W_c (\sigma_v^2 \hat{\Sigma}_c^{-1} + W_c^\top W_c)^{-1} W_c^\top \right) \end{aligned} \quad (57)$$

$$= \mathcal{K}_{\text{cal}} + \Delta \hat{\mathcal{K}}, \quad (58)$$

where

$$\begin{aligned} \Delta \hat{\mathcal{K}} &= \hat{E}_i[b_i c_i^\top] W_c^\top \\ &\quad - \hat{E}_i[b_i c_i^\top] W_c^\top W_c (\sigma_v^2 \hat{\Sigma}_c^{-1} + W_c^\top W_c)^{-1} W_c^\top. \end{aligned} \quad (59)$$

Substituting Eqs. (51)-(54) into Eqs. (28), (31) and (33), we obtain

$$\hat{\mathcal{K}}_{\text{dec}} \xrightarrow{J_{\text{tr}} \rightarrow \infty} \mathcal{K}_{\text{cal}}. \quad (60)$$

The limiting values of $\hat{\mathcal{K}}_{\text{dec}}$ and $\hat{\mathcal{K}}_{\text{dec}}^-$ differ by $\Delta\hat{\mathcal{K}}$, which goes to zero as $J_{\text{tr}} \rightarrow \infty$, since b_i and c_i are independent with zero-mean. Note that $\hat{\mathcal{K}}$ only depends on the training set and is a constant when during testing. Thus,

$$\begin{aligned}
 & \lim_{J_{\text{tr}} \rightarrow \infty} \text{MSE}_{\text{cal}}(\hat{\mathcal{K}}_{\text{dec}}^-) - \lim_{J_{\text{tr}} \rightarrow \infty} \text{MSE}_{\text{cal}}(\hat{\mathcal{K}}_{\text{dec}}) \\
 &= \mathbb{E} \left[\|g_{i,j} - \mathcal{K}_{\text{cal}} X_{i,j} - \Delta\hat{\mathcal{K}} X_{i,j}\|_2^2 \right. \\
 &\quad \left. - \|g_{i,j} - \mathcal{K}_{\text{cal}} X_{i,j}\|_2^2 \right] \\
 &= \text{tr} \left\{ \mathbb{E} \left[- (g_{i,j} - \mathcal{K}_{\text{cal}} X_{i,j}) X_{i,j}^\top \Delta\hat{\mathcal{K}}^\top \right. \right. \\
 &\quad \left. \left. - \Delta\hat{\mathcal{K}}^\top X_{i,j} (g_{i,j} - \mathcal{K}_{\text{cal}} X_{i,j})^\top \right. \right. \\
 &\quad \left. \left. + \Delta\hat{\mathcal{K}} X_{i,j} X_{i,j}^\top \Delta\hat{\mathcal{K}} \right] \right\} \\
 &= \text{tr} \{ \Delta\hat{\mathcal{K}} \Sigma_X \Delta\hat{\mathcal{K}}^\top \},
 \end{aligned} \tag{61}$$

where the last equality holds by noting that \mathcal{K}_{cal} is the optimal estimator of $g_{i,j}$ for $X_{i,j}$, which implies that the estimation error is orthogonal to the data $X_{i,j}$. Since the autocorrelation matrix Σ_X is positive semidefinite, $\Delta\hat{\mathcal{K}} \Sigma_X \Delta\hat{\mathcal{K}}^\top \geq 0$, which completes the proof. \square

Referring to the proof, we can see that $\hat{\mathcal{K}}_{\text{dec}} \xrightarrow{J_{\text{tr}} \rightarrow \infty} \mathcal{K}_{\text{cal}}$ whether or not $W_t^\top W_c = \mathbf{0}$. Since \mathcal{K}_{cal} minimizes MSE_{cal} , it is always true that

$$\lim_{J_{\text{tr}} \rightarrow \infty} \text{MSE}_{\text{cal}}(\hat{\mathcal{K}}_{\text{dec}}) \leq \lim_{J_{\text{tr}} \rightarrow \infty} \text{MSE}_{\text{cal}}(\hat{\mathcal{K}}_{\text{dec}}^-). \tag{62}$$

6.1 Simulation

To examine the performance $W_t^\top W_c \neq \mathbf{0}$, we simulated the model in Eqs. (5) and (6) with $s = 100$, $p = 10$, $\Sigma_c = 36\mathbf{I}$, $\Sigma_v = 4\mathbf{I}$ and $\Sigma_b = 4\mathbf{I}$, but with $t_{i,j} \sim \mathcal{U}(-30, 30)$ to better match the actual distribution of gaze in our other datasets.

We ran simulations for four different values (0, 0.2, 0.4 and 0.6) of $\|W_t^\top W_c\|$ where we used the max norm $\|A\| = \max_{i,j} |a_{i,j}|$. For all four cases, the matrix W_t was the same: a randomly generated matrix whose two columns were of unit length. For the case $\|W_t^\top W_c\| = 0$, the matrix W_c was randomly generated with p unit length columns orthogonal to the columns of W_t . For the other values of $\|W_t^\top W_c\|$, the matrix W_c was generated by taking the original W_c matrix and randomly adding or subtracting one of the columns from W_t scaled by the the desired value of $\|W_t^\top W_c\|$.

For each value of $\|W_t^\top W_c\|$, we examined the performance of the four different combinations of training (dec, dec) and testing (cal, cal), as I_{tr} varied. In each case, we ran 500 trials with $J_{\text{tr}} = 50$ randomly generated image-gaze pairs per subject. For testing, we used the same test set with 300 subjects and 1,000 images per subject.

Fig. 10 plots the simulation results. Consistent with Theorem 1, when $\|W_t^\top W_c\| = 0$ (Fig. 10(a)), the errors when training without and with gaze decomposition converge to the same value as I_{tr} increases (compare the red and blue curves), whether or not calibration is used in testing (for both the solid and dashed curves). Testing with calibration is better than testing without calibration (compare the solid and dashed curves). Consistent with Theorem 2, when

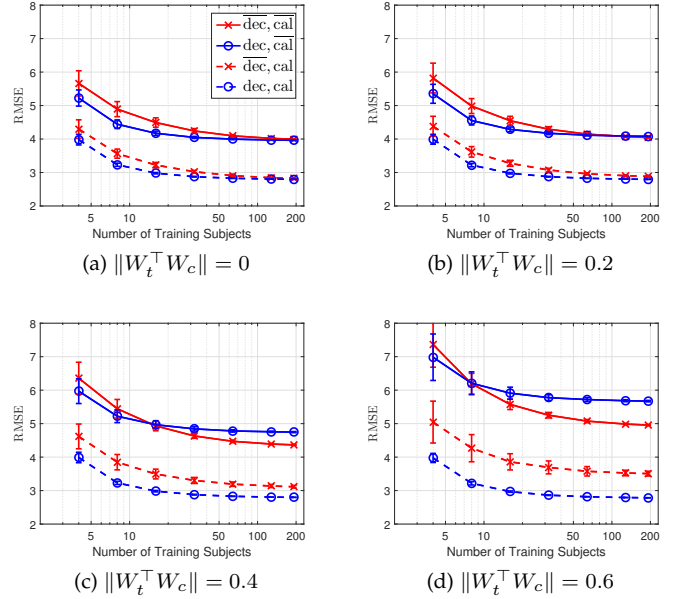


Fig. 10. Simulated testing results of $\hat{\mathcal{K}}$ and $\hat{\mathcal{K}}_{\text{dec}}$ under different values of $\|W_t^\top W_c\|$. Solid (dashed) lines indicated testing without (with) calibration. Red lines with \times markers (blue lines with \circ markers) indicate training without (with) gaze decomposition. RMSE means Root Mean Square Error. Error bars indicate standard deviations over 500 trials.

tested without calibration (solid curves), the performance of the estimator trained with gaze decomposition (blue) is better than that of the estimator trained without (red).

Consistent with Eq. (62), which holds for all values of $\|W_t^\top W_c\|$, when tested with calibration (dashed curves), the performance of the estimator trained with gaze decomposition (blue) is better than that of the estimator trained without (red), independent of the value of I_{tr} . As $\|W_t^\top W_c\|$ increases, the advantage of using the gaze decomposition increases (the dashed blue and red curves separate by more and more).

Consistent with Eq. (37), when testing without calibration (solid curves) and for large values of I_{tr} , the estimator trained without gaze decomposition (red) eventually performs better than the estimator trained with calibration (blue), and the performance mismatch increases with $\|W_t^\top W_c\|$. However, if the value of I_{tr} is small enough, the estimator with gaze decomposition performs better. The value of I_{tr} at which the two curves cross over increases as $\|W_t^\top W_c\|$ decreases. According to Theorem 2, when $\|W_t^\top W_c\| = 0$, the crossover is when $I_{\text{tr}} = \infty$.

7 CONCLUSION

We propose to use dilated-convolutions and a gaze decomposition method for appearance-based gaze estimation. Our results indicate that the proposed approach outperforms the state-of-the-art methods without ensembling and calibration on the MPIIGaze and EYEDIAP datasets by more than 6.3%.

We also propose a MAP-based calibration method to estimate the subject-dependent bias from a calibration set with low complexity, i.e., the number of gaze target and/or the number of images per target are small. The proposed

algorithm outperforms the state-of-the-art methods on MPIIGaze, EYEDIAP, ColumbiaGaze and NISLGaze when the calibration set is of low complexity, i.e., SGTC and MGTC with number of images fewer than or equal to 32. Particularly, SGTC reduced the estimation error significantly while only requiring a few samples (about 9) looking at one gaze target for calibration.

We are particularly interested in SGTC because it has two main advantages compared to MGTC: First, SGTC is simpler and less time-consuming as it only requires the user to gaze at one target. Second, it is more widely applicable. In some situations, e.g. screen-free applications, it is difficult to guide the user to look at multiple targets for MGTC. However, with SGTC, the camera is always a visible calibration target. Although there exists a performance gap between SGTC and MGTC, we believe that SGTC provides a practically useful way to improve accuracy.

We use a linear Gaussian model of image formation to analyze the proposed gaze decomposition. We theoretically and numerically demonstrate that with calibration, the estimator with gaze decomposition always achieves lower MSE compared to the estimator without gaze decomposition. While this might be expected, our theoretical analysis also sheds light on one of our more surprising experimental results: training with gaze decomposition improves performance even when calibration is not used when the number of training subjects is small. In general, we would not expect this due to the mismatch between the training and testing conditions. However, our theoretical analysis suggests that this is because subject-dependent variations in appearance and gaze dependent variations in appearance lie in orthogonal subspaces.

Finally, we introduce a new large-scale dataset, NISLGaze, which covers large variations of head pose and face location. We believe that the availability of NISLGaze will help to advance the evaluation and training of appearance-based gaze estimator, as the subject may appear at any camera location with any head pose in real-world applications. We also evaluate SGTC on NISLGaze in a more realistic setting, i.e. using consecutive frames when the subject is gazing at the camera. We think that this is a highly desirable and convenient calibration protocol for real-world applications.

APPENDIX A

WITHIN-DATASET EVALUATION ON EYEDIAP

To evaluate the performance of calibration, we conducted leave-one-subject-out cross-validation on the VGA videos of continuous screen target. We used data from both static and dynamic head pose. The videos were at 15 fps, resulting in about 3,500 images for each subject. We used these data because they had sufficient annotation to remove outliers, e.g. images during blinking.

The results are shown in Fig. 11 and Fig. 12. In Fig. 11, SGTC reduced the error significantly. For example, a 1.1° (23.4%) improvement was achieved when calibrated on only 9 samples. On average, the gap between SGTC and MGTC was about 0.5° (10.6% of the error achieved by the estimator without calibration). As shown in Fig. 12, 0.7° (14.9%) to 1.4° (31.9%) improvement was achieved across different locations. The SD across locations was 0.2° .

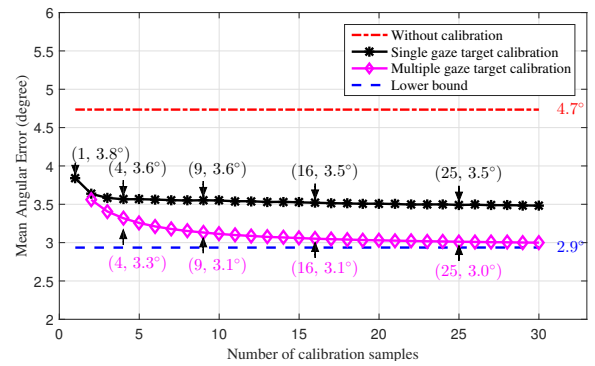


Fig. 11. Mean angular error in camera coordinates as a function of number of calibration samples on the EYEDIAP dataset.

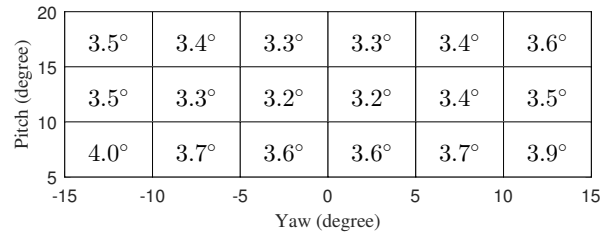


Fig. 12. Mean angular error of SGTC ($S = 9$) when the gaze target is located within different 5×5 regions on EYEDIAP. $\bar{E} = 4.7^\circ$, $\underline{E} = 2.9^\circ$.

TABLE 7
Single Gaze Target Calibration on EYEDIAP ($T = 1$, $S = 9$).

Method	Error
LP [36]	3.9°
DF [43]	4.0°
Dilated + GD	3.6°

Table 7 compares our method to LP and DF in terms of the estimation error after calibration ($T = 1$, $S = 9$). Our method outperformed them.

REFERENCES

- [1] R. Menges, C. Kumar, D. Müller, and K. Sengupta, "Gazetheweb: A gaze-controlled web browser," in *Proceedings of the Web for All Conference on The Future of Accessible Work*. ACM, 2017, p. 25. 1
- [2] J. Pi and B. E. Shi, "Probabilistic adjustment of dwell time for eye typing," in *International Conference on Human System Interactions*. IEEE, 2017, pp. 251–257. 1
- [3] C.-M. Huang and B. Mutlu, "Anticipatory robot control for efficient human-robot collaboration," in *ACM/IEEE International Conference on Human Robot Interaction*. IEEE, 2016, pp. 83–90. 1
- [4] A. Grillini, D. Ombelet, R. S. Soans, and F. W. Cornelissen, "Towards using the spatio-temporal properties of eye movements to classify visual field defects," in *Proceedings of the ACM Symposium on Eye Tracking Research & Applications*. ACM, 2018, p. 38. 1
- [5] B. I. Outram, Y. S. Pai, T. Person, K. Minamizawa, and K. Kunze, "Anyorbit: Orbital navigation in virtual environments with eye-tracking," in *Proceedings of the ACM Symposium on Eye Tracking Research & Applications*. ACM, 2018, p. 45. 1
- [6] A. Patney, M. Salvi, J. Kim, A. Kaplanyan, C. Wyman, N. Bentley, D. Luebke, and A. Lefohn, "Towards foveated rendering for gaze-tracked virtual reality," *ACM Transactions on Graphics*, vol. 35, no. 6, p. 179, 2016. 1
- [7] S. Hoppe, T. Loetscher, S. A. Morey, and A. Bulling, "Eye movements during everyday behavior predict personality traits," *Frontiers in Human Neuroscience*, vol. 12, p. 105, 2018. 1

- [8] S. L. Rogers, C. P. Speelman, O. Guidetti, and M. Longmuir, "Using dual eye tracking to uncover personal gaze patterns during social interaction," *Scientific reports*, vol. 8, no. 1, pp. 1–9, 2018. **1**
- [9] E. Brau, J. Guan, T. Jeffries, and K. Barnard, "Multiple-gaze geometry: Inferring novel 3d locations from gazes observed in monocular video," in *Proceedings of the European Conference on Computer Vision*. Springer, 2018, pp. 641–659. **1**
- [10] E. Chong, N. Ruiz, Y. Wang, Y. Zhang, A. Rozga, and J. M. Rehg, "Connecting gaze, scene, and attention: Generalized attention estimation via joint modeling of gaze and scene saliency," in *Proceedings of the European Conference on Computer Vision*. Springer, 2018, pp. 397–412. **1**
- [11] W. Fuhl, D. Geisler, T. Santini, T. Appel, W. Rosenstiel, and E. Kasneci, "Cbf: Circular binary features for robust and real-time pupil center detection," in *Proceedings of the ACM Symposium on Eye Tracking Research & Applications*. ACM, 2018, p. 8. **1**
- [12] H. Wang, J. Pi, T. Qin, S. Shen, and B. E. Shi, "SLAM-based localization of 3D gaze using a mobile eye tracker," in *Proceedings of the ACM Symposium on Eye Tracking Research & Applications*. ACM, 2018, p. 65. **1**
- [13] J. Pi and B. E. Shi, "Task-embedded online eye-tracker calibration for improving robustness to head motion," in *Proceedings of the 11th ACM Symposium on Eye Tracking Research & Applications*. ACM, 2019, p. 8. **1**
- [14] X. Zhang, Y. Sugano, M. Fritz, and A. Bulling, "MPIIGaze: Real-world dataset and deep appearance-based gaze estimation," *IEEE Transactions on Pattern Analysis and Machine Intelligence*, vol. 41, no. 1, pp. 162–175, 2019. **1, 2, 6**
- [15] —, "Appearance-based gaze estimation in the wild," in *Proceedings of the IEEE Conference on Computer Vision and Pattern Recognition*, 2015, pp. 4511–4520. **1, 2, 3, 4, 5, 6**
- [16] T. Fischer, H. J. Chang, and Y. Demiris, "Rt-gene: Real-time eye gaze estimation in natural environments," in *Proceedings of European Conference on Computer Vision*. Springer, 2018, pp. 339–357. **1, 3, 6, 7**
- [17] K. A. Funes Mora, F. Monay, and J.-M. Odobez, "Eyediap: A database for the development and evaluation of gaze estimation algorithms from rgb and rgb-d cameras," in *Proceedings of the Symposium on Eye Tracking Research and Applications*. ACM, 2014, pp. 255–258. **1, 3, 5, 6**
- [18] Z. He, A. Spurr, X. Zhang, and O. Hilliges, "Photo-realistic monocular gaze redirection using generative adversarial networks," in *Proceedings of the IEEE International Conference on Computer Vision*, 2019. **1, 3**
- [19] K. Krafka, A. Khosla, P. Kellnhofer, H. Kannan, S. Bhandarkar, W. Matusik, and A. Torralba, "Eye tracking for everyone," in *Proceedings of the IEEE Conference on Computer Vision and Pattern Recognition*, 2016, pp. 2176–2184. **1, 2, 3, 4, 6, 7**
- [20] A. Shrivastava, T. Pfister, O. Tuzel, J. Susskind, W. Wang, and R. Webb, "Learning from simulated and unsupervised images through adversarial training," in *Proceedings of the IEEE International Conference on Computer Vision*. IEEE, 2017, pp. 2242–2251. **1, 3**
- [21] B. A. Smith, Q. Yin, S. K. Feiner, and S. K. Nayar, "Gaze locking: Passive eye contact detection for human-object interaction," in *Proceedings of the ACM Symposium on User Interface Software and Technology*. ACM, 2013, pp. 271–280. **1, 3, 6**
- [22] Y. Sugano, Y. Matsushita, and Y. Sato, "Learning-by-synthesis for appearance-based 3D gaze estimation," in *Proceedings of the IEEE Conference on Computer Vision and Pattern Recognition*. IEEE, 2014, pp. 1821–1828. **1, 2, 3**
- [23] K. Wang, R. Zhao, and Q. Ji, "A hierarchical generative model for eye image synthesis and eye gaze estimation," in *Proceedings of the IEEE Conference on Computer Vision and Pattern Recognition*, June 2018, pp. 440–448. **1, 3**
- [24] E. Wood, T. Baltrušaitis, L.-P. Morency, P. Robinson, and A. Bulling, "Learning an appearance-based gaze estimator from one million synthesised images," in *Proceedings of the ACM Symposium on Eye Tracking Research & Applications*. ACM, 2016, pp. 131–138. **1, 3**
- [25] Z. Chen and B. E. Shi, "Appearance-based gaze estimation using dilated-convolutions," in *Asian Conference on Computer Vision*. Springer, 2018, pp. 309–324. **1, 3, 4, 6, 7**
- [26] Y. Cheng, F. Lu, and X. Zhang, "Appearance-based gaze estimation via evaluation-guided asymmetric regression," in *Proceedings of the European Conference on Computer Vision*. Springer, 2018, pp. 105–121. **1, 2**
- [27] H. Deng and W. Zhu, "Monocular free-head 3d gaze tracking with deep learning and geometry constraints," in *Proceedings of the IEEE International Conference on Computer Vision*. IEEE, 2017, pp. 3162–3171. **1, 2**
- [28] D. Lian, L. Hu, W. Luo, Y. Xu, L. Duan, J. Yu, and S. Gao, "Multiview multitask gaze estimation with deep convolutional neural networks," *IEEE Transactions on Neural Networks and Learning Systems*, pp. 1–14, 2018. **1, 2**
- [29] C. Palmero, J. Selva, M. A. Bagheri, and S. Escalera, "Recurrent cnn for 3d gaze estimation using appearance and shape cues," in *British Machine Vision Conference*, 2018. **1, 2, 6, 7**
- [30] V. Parekh, R. Subramanian, and C. Jawahar, "Eye contact detection via deep neural networks," in *International Conference on Human-Computer Interaction*. Springer, 2017, pp. 366–374. **1, 2**
- [31] R. Ranjan, S. De Mello, and J. Kautz, "Light-weight head pose invariant gaze tracking," in *IEEE Conference on Computer Vision and Pattern Recognition Workshops*. IEEE, 2018, pp. 2156–2164. **1, 2**
- [32] Y. Xiong, H. J. Kim, and V. Singh, "Mixed effects neural networks (menets) with applications to gaze estimation," in *Proceedings of the IEEE Conference on Computer Vision and Pattern Recognition*, 2019, pp. 7743–7752. **1, 2**
- [33] X. Zhang, Y. Sugano, M. Fritz, and A. Bulling, "Its written all over your face: Full-face appearance-based gaze estimation," in *IEEE Conference on Computer Vision and Pattern Recognition Workshops*. IEEE, 2017, pp. 2299–2308. **1, 2, 5, 6, 7**
- [34] F. Yu and V. Koltun, "Multi-scale context aggregation by dilated convolutions," *arXiv preprint arXiv:1511.07122*, 2015. **1**
- [35] L.-C. Chen, G. Papandreou, F. Schroff, and H. Adam, "Rethinking atrous convolution for semantic image segmentation," *arXiv preprint arXiv:1706.05587*, 2017. **1**
- [36] E. Lindén, J. Sjöstrand, and A. Proutiere, "Learning to personalize in appearance-based gaze tracking," in *IEEE International Conference on Computer Vision Workshops*, 2019. **1, 2, 7, 8, 10, 14**
- [37] T. Schneider, B. Schauerte, and R. Stiefelhagen, "Manifold alignment for person independent appearance-based gaze estimation," in *International Conference on Pattern Recognition*. IEEE, 2014, pp. 1167–1172. **2**
- [38] Y. Yu, G. Liu, and J.-M. Odobez, "Deep multitask gaze estimation with a constrained landmark-gaze model," in *European Conference on Computer Vision Workshops*. Springer, 2018, pp. 456–474. **2**
- [39] S. Park, A. Spurr, and O. Hilliges, "Deep pictorial gaze estimation," in *Proceedings of the European Conference on Computer Vision*. Springer, 2018, pp. 741–757. **2**
- [40] E. D. Guestrin and M. Eizenman, "General theory of remote gaze estimation using the pupil center and corneal reflections," *IEEE Transactions on Biomedical Engineering*, vol. 53, no. 6, pp. 1124–1133, 2006. **2, 3**
- [41] G. Liu, Y. Yu, K. A. Funes-Mora, J.-M. Odobez, and E. T. SA, "A differential approach for gaze estimation with calibration," in *British Machine Vision Conference*, 2018. **2, 7**
- [42] X. Zhang, Y. Sugano, and A. Bulling, "Evaluation of appearance-based methods and implications for gaze-based applications," in *Proceedings of the CHI Conference on Human Factors in Computing Systems*. ACM, 2019, p. 416. **2, 7**
- [43] G. Liu, Y. Yu, K. A. F. Mora, and J.-M. Odobez, "A differential approach for gaze estimation," *IEEE Transactions on Pattern Analysis and Machine Intelligence*, 2019. **2, 7, 8, 10, 14**
- [44] Y. Yu, G. Liu, and J.-M. Odobez, "Improving few-shot user-specific gaze adaptation via gaze redirection synthesis," in *Proceedings of the IEEE Conference on Computer Vision and Pattern Recognition*, 2019, pp. 11937–11946. **2, 7, 8**
- [45] S. Park, S. De Mello, P. Molchanov, U. Iqbal, O. Hilliges, and J. Kautz, "Few-shot adaptive gaze estimation," in *Proceedings of the IEEE International Conference on Computer Vision*, 2019. **2, 7, 8**
- [46] D. A. Atchison and G. Smith, *Optics of the human eye*. Oxford: Butterworth-Heinemann, 2000. **3**
- [47] X. Zhang, Y. Sugano, and A. Bulling, "Revisiting data normalization for appearance-based gaze estimation," in *Proceedings of the ACM Symposium on Eye Tracking Research & Applications*. ACM, 2018, p. 12. **4, 5, 10**
- [48] D. E. King, "Dlib-ml: A machine learning toolkit," *Journal of Machine Learning Research*, vol. 10, pp. 1755–1758, 2009. **4**
- [49] T. Baltrušaitis, A. Zadeh, Y. C. Lim, and L.-P. Morency, "OpenFace 2.0: Facial behavior analysis toolkit," in *IEEE International Conference on Automatic Face & Gesture Recognition*. IEEE, 2018, pp. 59–66. **4, 6**

- [50] K. Simonyan and A. Zisserman, "Very deep convolutional networks for large-scale image recognition," *arXiv preprint arXiv:1409.1556*, 2014. 4
- [51] J. Deng, W. Dong, R. Socher, L.-J. Li, K. Li, and L. Fei-Fei, "Imagenet: A large-scale hierarchical image database," in *Proceedings of the IEEE Conference on Computer Vision and Pattern Recognition*. IEEE, 2009, pp. 248–255. 4
- [52] S. Ioffe, "Batch renormalization: Towards reducing minibatch dependence in batch-normalized models," in *Advances in Neural Information Processing Systems*, 2017, pp. 1942–1950. 4
- [53] Z. Chen and B. E. Shi, "Offset calibration for appearance-based gaze estimation via gaze decomposition," *Winter Conference on Applications of Computer Vision*, 2020. 5, 7, 8
- [54] J. Cech and T. Soukupova, "Real-time eye blink detection using facial landmarks," *Computer Vision Winter Workshop*, 2016. 6
- [55] T. Kailath, A. H. Sayed, and B. Hassibi, *Linear estimation*. Prentice Hall, 2000. 11
- [56] M. A. Woodbury, "Inverting modified matrices," *Memorandum Report*, 1950. 12